Erschienen in: Optics Letters ; 47 (2022), 14. - S. 3552-3555
https://dx.doi.org/10.1364/OL.461076

Passively phase-locked Er:fiber source of single-cycle pulses in the near infrared with electro-optic timing modulation for field-resolved electron control

Christoph Schoenfeld,[1] Philipp Sulzer,[1] Daniele Brida,[1,2] Alfred Leitenstorfer,[1] and Takayuki Kurihara[1,3,*]

[1] *Department of Physics and Center for Applied Photonics, University of Konstanz, D-78457 Konstanz, Germany*
[2] *Department of Physics and Materials Science, Université du Luxembourg, 162a Avenue de la Faïencerie, L-1511 Luxembourg, Luxembourg*
[3] *Institute for Solid State Physics, The University of Tokyo, 5-1-5 Kashiwanoha, Kashiwa, Chiba, 272-8581, Japan*
**Corresponding author: takayuki.kurihara@issp.u-tokyo.ac.jp*

A single-cycle light source in the near infrared is demonstrated enabling sensitive applications of ultrafast optical field control of electronic transport. The compact Er:fiber system generates passively phase-locked pulses with broadband spectra covering 150 THz to 350 THz at a duration of 4.2 fs and 40 MHz repetition rate. A second output arm is equipped with an electro-optic modulator (EOM) that switches the arrival time of the pulses by 700 ps at arbitrary frequencies up to 20 MHz, enabling timing modulation of the pump pulse without changing the average intensity. As a benchmark demonstration, we investigate the carrier relaxation dynamics in low-temperature-grown InGaAs (LT-InGaAs) using quantum interference currents (QuICs).

Subcycle optical control of the directionality of charge currents in solid-state devices bears the potential for achieving ultrafast processing speed in future electronics. Recent efforts achieving this goal of high-bandwidth injection and readout have been due to the availability of optical pulses lasting only one oscillation of the electric field [1,2]. Their intrinsic symmetry break of the incident field in combination with manipulation of the carrier-envelope phase (CEP) has enabled them to drive electronic transport in various condensed-matter or nanoscopic systems. Examples are field-induced tunneling currents between metallic contacts on femtosecond to attosecond timescales [1,2], electronic field-emission from surfaces [3–5], and quantum interference currents (QuICs) in semiconductors [6–9] and dielectric materials [10,11].

In many of these cases, the required field strength is substantially lower than the one required for typical strong-field experiments such as high-harmonics generation from atoms [12]. Even minute pulse energies below 1 nJ available at multi-MHz repetition rates may be sufficient for field-induced transport in a single-electron regime [1,2]. At such high repetition rates, a technical challenge arises when one combines ultrafast experiments on single-electron systems or scanning tunneling microscopy [13–15] with optical pumping. Since the intrapulse distance becomes comparable to the timescales for electronic decay and heat dissipation, simply modulating the pump intensity might strongly contaminate the signals originating directly from ultrafast electronic processes. To resolve this challenge, the scheme of timing modulation may be exploited [16,17]. This relies on switching the arrival time of the pump pulse before and after the probe pulse without reducing the repetition rate of the excitation. In this way, the offset contribution of the pump-probe signal due to long-lifetime components is subtracted, enabling, for example, the dynamical observation of individual excitons under strong spatial confinement [18].

Here, we implement a fully optoelectronically controlled timing-modulation scheme into a single-cycle light source with passive CEP stability. The final aim is to perform field-resolved optical experiments on femtosecond and attosecond nonlinear transport phenomena [13,15,19]. The laser system consists of three major parts, as shown schematically in Fig. 1. The red panel highlights the experimental setup for the generation of a passively phase-locked frequency comb. First, an InGaAs saturable absorber-based, self-starting all-fiber solitonic erbium oscillator (Er:Osc) emits a pulse train at a repetition rate f_{rep} = 40 MHz with a central frequency of 192 THz, spectral bandwidth of 1.22 THz, and a pulse duration of 300 fs [1,3]. The pulse energies are then boosted from 33 pJ to 9.2 nJ in a subsequent erbium-doped fiber amplifier (EDFA). The amplified pulses are temporally compressed by a pair of silicon prisms and sent into a germanosilicate highly nonlinear fiber (HNF) with a core diameter of 3.5 µm. Interplay between self-phase modulation and dispersion results in a tailored coherent supercontinuum spanning from the dispersive wave centered at 352 THz to the soliton at 159 THz (inset within red frame in Fig. 1). Difference frequency generation (DFG) between these two spectral components in periodically poled lithium niobate (PPLN) with 0.5 mm thickness results in efficient back conversion into

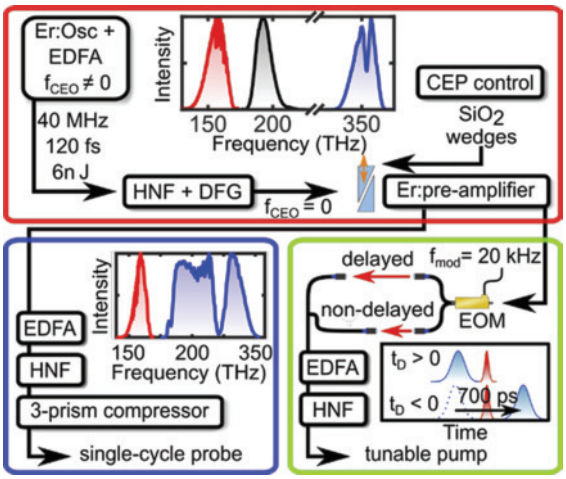

Fig. 1. Schematic of the experimental setup. Top (red panel): Passive elimination of f_{CEO} by DFG (black curve of the inset) between a dispersive (blue) and a solitonic wave (red). Bottom left (blue panel): Setup for generation of single-cycle probe pulses. Inset: output spectra after 3-prism compressor. Bottom right (green panel): Setup for timing modulation of the pump by an electro-optic modulator (EOM).

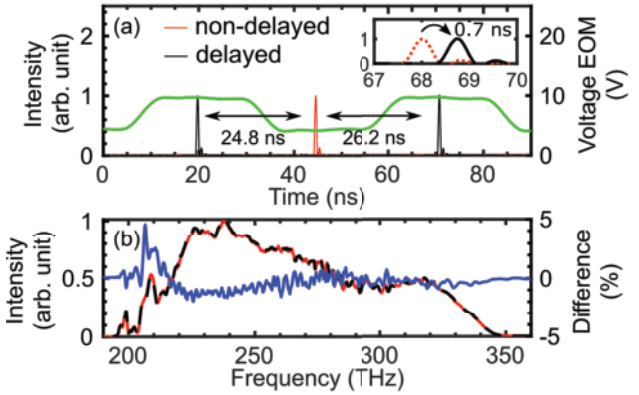

Fig. 2. (a) Pulse train output from the pump branch measured with an oscilloscope at a timing-modulation frequency of 20 MHz. Inset: zoom-in around 67–70 ns, where the non-delayed pulse (red dotted line) is shifted by 25.5 ns ($1/f_{rep}$) to highlight the difference of arrival time from the delayed (black) pulse. (b) Intensity spectra corresponding to each path in (a), obtained after broadening by HNF. Blue spectrum shows the difference between the delayed and non-delayed outputs.

the erbium gain window at 193 THz. This step eliminates the carrier-envelope offset frequency (f_{CEO}), passively stabilizing the CEP which can be controlled by the insertion of a pair of fused-silica wedges. The DFG output is first amplified and then split for separate seeding of the pump and probe amplifier stages.

The green box in Fig. 1 features the pump branch. The key module is a fiber-coupled electro-optic modulator (EOM). Depending on the applied voltage, it switches one of the two free-space pathways that have a 21 cm difference of propagation lengths, resulting in a relative retardation of 700 ps. The inset schematically depicts the arrival times of such pulses (blue) compared to the probe which remains fixed (red). Here, the pulse order at $t_D > 0$ and $t_D < 0$ correspond to the pump-on and pump-off states, respectively. After recombination by a 50/50 fiber coupler, the timing-modulated pump pulses are amplified by an EDFA and compressed by a silicon prism pair. Another HNF generates a tailorable supercontinuum with a spectrum covering the interval between 150 and 350 THz at a pulse energy of 0.7 nJ. This output is compressed to a pulse duration in the order of tens of femtoseconds by a pair of SF10 prisms.

Figure 2(a) illustrates a typical oscilloscope trace of the pulse trains timing-modulated at the Nyquist frequency of 20 MHz. Here, the delayed (black) and non-delayed (red) transients are measured separately by optically blocking the other path and detecting the pulses with a photodiode at the output of the HNF. The voltage applied to the EOM (green) triggers the oscilloscope, so that the relative timing of the two pulse trains with respect to each other is correctly recorded. Depending on the applied voltage, the distances between the pulses are set to 24.8 ns or 26.2 ns. The difference of 1.4 ns corresponds to twice the 700 ps retardation introduced by the free-space part. The final pump spectra from the HNF are plotted in Fig. 2(b). Here, we selected the desired path by applying constant voltages of 10 V or 4 V to the EOM. The overall spectral difference between the delayed and non-delayed pulses is typically below 1-2% within 220 to 350 THz, ensuring negligible difference in the total energy and pulse duration between the two pulse trains when used as pump. This excellent modulation quality is expected to greatly suppress any slow parasitic artifacts in nanoscale field-dependent transport experiments such as heat-induced expansion of metallic tunneling tips [20].

The blue frame in Fig. 1 depicts the probe branch. In contrast to the pump, the supercontinuum bandwidth is maximized to cover more than one octave by optimizing the length of HNF and carefully tuning the Si prism insertion. Figure 3(a) shows the amplitude spectra obtained from an optical spectrum analyzer (OSA) and a phase spectrum measured by second harmonics frequency-resolved optical gating (SH-FROG). Based on a bandwidth of 192 THz ($1/e^2$), dispersion control by a three-prism compressor [2] results in a pulse duration as short as 4.2 fs at full-width at half-maximum (FWHM), corresponding to one oscillation cycle of the carrier frequency of 233 THz. Figure 3(b) depicts the reconstructed waveform for a cosine-like phase (CEP = 0) of the electric field. The asymmetry between the positive and negative peaks of the electric field waveform reaches $|E_{min}/E_{max}| \sim 0.71$, which is expected to suffice for inducing a considerable static polarization in a variety of nonlinear processes [1,2,21]. The energy of the single-cycle pulse amounts to 2 nJ, of which 45% is confined within the FWHM.

To monitor the CEP, a self-referencing f-to-2f interferometer is employed in the probe branch [22–24] by overlapping the 330 THz component of the fundamental supercontinuum and the second harmonic of the soliton around 165 THz. The interferogram is recorded while continuously inserting the fused-silica (FS) wedges as shown in Fig. 4(a). The modulation depth of a single interference fringe reaches 95%, indicating excellent CEP stability during the acquisition time (8 ms) of the spectrometer. The corresponding phase information extracted from the fringe pattern is shown in Fig. 4(b). Increasing the thickness of FS by 81 μm with the wedge corresponds to a linear phase shift of 2π.

Neither the bandwidth nor the temporal duration of the supercontinuum is affected by the mechanical movement of the wedge. Furthermore, we demonstrate active elimination of the long-term CEP variation by continuously feeding back the interferogram signal on the wedge position [Fig. 4(c)]. The fringe

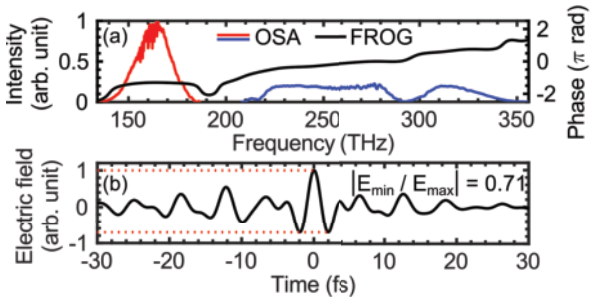

Fig. 3. (a) Intensity spectra of dispersive (blue) and solitonic components (red) of the supercontinuum after HNF of the probe branch, measured by OSA. Phase spectrum (black) is obtained by SH-FROG. (b) Time-domain electric field profile assuming a cosine-like phase, as obtained by Fourier transform of (a).

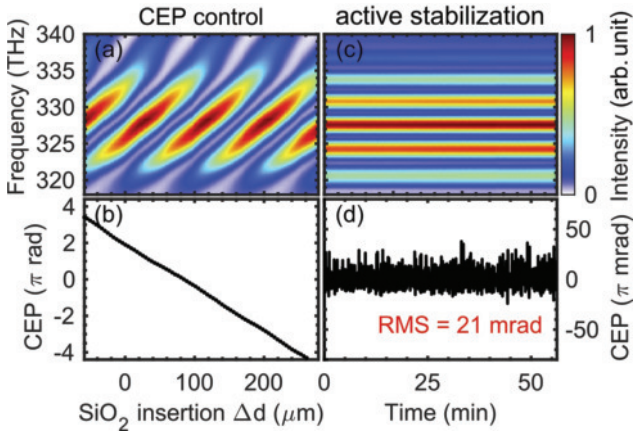

Fig. 4. Control and stabilization of the CEP: (a) f-to-2f interferogram while inserting the FS wedge. (b) Relative CEP as a function of the FS insertion. (c) Temporal evolution of the f-to-2f interferogram actively stabilized over 1 hour with a feedback bandwidth of 1.3 Hz. (d) Phase fluctuations extracted from (c).

pattern stays centered around 328 THz without noticeable fluctuation over 1 hour. Remaining phase fluctuations depicted in Fig. 4(d) amount to a root mean square deviation of only 21 mrad within the measured time window, indicating efficient suppression of slow phase drifts. This level of stability renders the system highly attractive for phase-sensitive subcycle spectroscopy such as optical field-induced scanning tunneling microscopy which usually takes tens of minutes for the signal to accumulate [13,15,19].

Next, we demonstrate the capability of our system in detecting photoinduced changes of the ultrafast transport dynamics in condensed-matter systems by timing modulation. We study QuICs in low-temperature-grown InGaAs (LT-InGaAs), using the $\omega \sim 160$ THz and $2\omega \sim 320$ THz spectral components of the probe branch. QuIC originates from the difference in parity of the transition dipoles induced by one-photon (1PA) and two-photon (2PA) absorption [8,25,26]. Since 1PA alters the angular momentum quantum number L by ±1, while 0 or ±2 for 2PA, it results in an asymmetric electron distribution in k-space with a net current density. The induced current depends on the CEP as

$$\mathbf{J_{QuIC}} \sim \mathbf{I}_\omega \sqrt{\mathbf{I}_{2\omega}}\, \mathbf{sin}(\mathbf{\Phi_{CEP}}), \qquad (1)$$

where I_ω and $I_{2\omega}$ describe the intensities of the ω and 2ω components of the incident light [8,27]. Our sample is a 630 μm thick LT-InGaAs substrate [Fig. 5 (a): BATOP GmbH, bPCA-100-05-10-1060-0]. It has a direct bandgap of $E_g = 1.17$ eV = 283 THz, fulfilling the condition for QuIC ($2\hbar\omega = 320$ THz$<E_g<\hbar\omega =$ 160 THz). The probe pulse is linearly polarized along the gold electrode gap while the pump is set orthogonally to avoid unwanted 1PA interference. The spectral components from 180 to 300 THz in the probe pulse are filtered out in the Fourier plane of the prism compressor to exploit only the spectral components contributing to QuIC [Fig. 5(b)]. Both beams are focused to a spot size of approximately 4 μm into the 5 μm electrode gap. The current from the electrodes is amplified and then detected by a lock-in amplifier.

First, a CEP dependence of the current induced only by the probe pulse without the pump is measured by mechanically chopping the solitonic wave of the probe pulse at approximately 0.7 kHz. The result is depicted in Fig. 5(c). A sinusoidal dependence along with the reversal of the current direction for a phase shift by multiples of π clearly matches the behavior expected from Eq. (1) and demonstrates generation of a QuIC. Next, the chopper is removed and the pump pulse is turned on with timing-modulation frequency at 20 kHz with a duty cycle of 50%. At this modulation frequency, the combined noise level of the transimpedance amplifier and laser fluctuations is minimal. The resulted pump-induced change ΔJ_{QuIC} of the QuIC signal is plotted in Fig. 5(d) for various time delays t_D between the pump and probe pulses using a mechanical delay line. A prominent change in the amplitude is observed around the pump-probe overlap time $t_D = 0$. Figure 5(e) shows the contrast of the CEP-dependent component of Fig. 5(d) plotted as a function of the time delay t_D, extracted by a root mean square fit with sinusoidal functions. For time delays $t_D < 0$ (probe first), a finite contrast of QuIC is clearly observable as a constant offset. This contrast exponentially increases toward $t_D = 0$ with a time constant of $\tau_1 = (391 \pm 53)$ fs. Afterwards, it exponentially vanishes for $t_D > 0$ (pump first) with a decay time of $\tau_2 = (345 \pm 45)$ fs.

The increase of the QuIC amplitude near $t_D = 0$ can be understood by considering the Pauli blocking between the pump- and QuIC-induced electron populations [Fig. 5(f)]. When the conduction band is occupied by the pump-excited electrons, the absorption of the probe pulse at the same energy level is partially prohibited. This saturation effect uniformly reduces the QuIC efficiency, resulting in an enhanced contrast detected as the difference between pump on and off states via timing modulation. On this basis, the signal at $t_D > 0$ [right panel of Fig. 5(f)] is ascribed to intraband relaxation of the electrons excited by the pump pulses. Here, the pump-excited electrons occupy a wide energy spectrum in the conduction band due to the broadband pump spanning 180 to 320 THz. They subsequently lose energy by emitting optical phonons and decay toward the conduction band minima, emptying the occupation at higher energy levels. At this stage, the absorption of the probe photons around 320 THz fully revives, resulting in the complete loss of the difference signal compared with pump-off states.

The lifetime of $\tau_2 = (345 \pm 45)$ fs deduced from Fig. 5(d) roughly agrees with previously reported time constants of optical phonon emission in similar systems such as GaAs [28]. In the negative time region $t_D < 0$ [left panel of Fig. 5(f)], the QuIC carriers first populate a relatively narrow energy band at around an interband frequency of 320 THz and then relax down to E_g (283

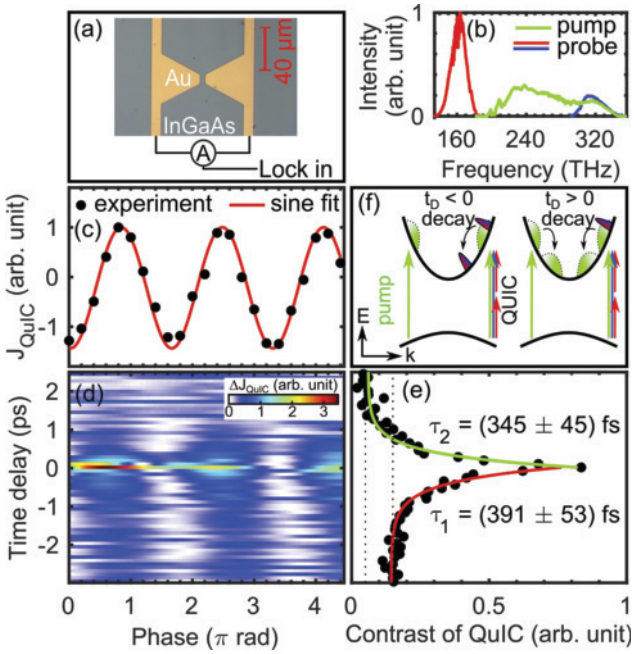

Fig. 5. QuIC in InGaAs. (a) Sample structure. (b) Pump and probe spectra. (c) Probe-induced J_{QuIC} measured without the pump. (d) Pump-induced change ΔJ_{QuIC} plotted against CEP and time delay t_D. (e) Time evolution of the extracted contrast of QuIC in (d). (f) Schematic of the photoexcited carrier relaxation dynamics in the conduction band for $t_D < 0$ and $t_D > 0$. The pump and the probe photons causing 1PA and 2PA are represented by green, blue and red arrows, respectively.

THz). In this case, however, as the broadband pump pulse (180 THz to 320 THz) subsequently excites the system, the energy levels of the pump-induced electrons always overlap with the relaxed probe-induced electrons at any delay times. Since the pump pulse excites carriers with an inversion-symmetric distribution, it reduces the anisotropy of the electronic population previously induced by the probe pulse via QuIC, resulting in the increased contrast upon lock-in detection. Therefore, the contrast of the QuIC signal persists as an offset over a long period for the $t_D < 0$ region. Thus, the observed time evolution of the contrast of QuIC can be consistently understood by considering the spectral overlap between the pump and probe pulses, decay dynamics of the photoexcited electrons, and Pauli-blocking effects.

In conclusion, we present an erbium-doped fiber-based light source combining a passively phase-locked single-cycle probe in the near infrared with a timing modulator for the pump pulses. As a first application, we revealed photoinduced bleaching dynamics of the QuIC signal in LT-InGaAs. The system presented here promises to become a powerful tool when applied to optical field-induced electron transport with subcycle temporal resolution in the future.

Funding. Deutsche Forschungsgemeinschaft (425217212, SFB 1432); European Research Council (819871); Japan Society for the Promotion of Science (JP20K22478, JP21K14550); European Regional Development Fund (2017-03-022-19).

Acknowledgments. T.K. received support from Japan Society for the Promotion of Science (JSPS) for the Postdoctoral Fellowship for Research Abroad, Zukunftskolleg Research Fellowship from the University of Konstanz. Support by TOPTICA Photonics AG is gratefully acknowledged.

Disclosures. The authors declare no conflicts of interest.

REFERENCES

1. T. Rybka, M. Ludwig, M. F. Schmalz, V. Knittel, D. Brida, and A. Leitenstorfer, Nat. Photonics **10**, 667 (2016).
2. M. Ludwig, G. Aguirregabiria, F. Ritzkowsky, T. Rybka, D. C. Marinica, J. Aizpurua, A. G. Borisov, A. Leitenstorfer, and D. Brida, Nat. Phys. **16**, 341 (2020).
3. P. Hommelhoff, Y. Sortais, A. Aghajani-Talesh, and M. A. Kasevich, Phys. Rev. Lett. **96**, 077401 (2006).
4. H. Yanagisawa, S. Schnepp, C. Hafner, M. Hengsberger, D. E. Kim, M. F. Kling, A. Landsman, L. Gallmann, and J. Osterwalder, Sci. Rep. **6**, 35877 (2016).
5. A. Tafel, S. Meier, J. Ristein, and P. Hommelhoff, Phys. Rev. Lett. **123**, 146802 (2019).
6. E. Dupont, P. B. Corkum, H. C. Liu, M. Buchanan, and Z. R. Wasilewski, Phys. Rev. Lett. **74**, 3596 (1995).
7. R. Atanasov, A. Haché, J. L. P. Hughes, H. M. van Driel, and J. E. Sipe, Phys. Rev. Lett. **76**, 1703 (1996).
8. A. Haché, Y. Kostoulas, R. Atanasov, J. L. P. Hughes, J. E. Sipe, and H. M. van Driel, Phys. Rev. Lett. **78**, 306 (1997).
9. T. M. Fortier, P. A. Roos, D. J. Jones, S. T. Cundiff, R. D. R. Bhat, and J. E. Sipe, Phys. Rev. Lett. **92**, 147403 (2004).
10. A. Schiffrin, T. Paasch-Colberg, N. Karpowicz, V. Apalkov, D. Gerster, S. Mühlbrandt, M. Korbman, J. Reichert, M. Schultze, S. Holzner, J. V. Barth, R. Kienberger, R. Ernstorfer, V. S. Yakovlev, M. I. Stockman, and F. Krausz, Nature **493**, 70 (2013).
11. V. Hanus, V. Csajbók, Z. Pápa, J. Budai, Z. Márton, G. Z. Kiss, P. Sándor, P. Paul, A. Szeghalmi, Z. Wang, B. Bergues, M. F. Kling, G. Molnár, J. Volk, and P. Dombi, in *Frontiers in Optics + Laser Science 2021* (Optica Publishing Group, 2021), FTh4B.5.
12. T. Brabec and F. Krausz, Rev. Mod. Phys. **72**, 545 (2000).
13. T. L. Cocker, D. Peller, P. Yu, J. Repp, and R. Huber, Nature **539**, 263 (2016).
14. Y. Luo, V. Jelic, G. Chen, P. H. Nguyen, Y.-J. R. Liu, J. A. M. Calzada, D. J. Mildenberger, and F. A. Hegmann, Phys. Rev. B **102**, 205417 (2020).
15. S. Yoshida, Y. Arashida, H. Hirori, T. Tachizaki, A. Taninaka, H. Ueno, O. Takeuchi, and H. Shigekawa, ACS Photonics **8**, 315 (2021).
16. Y. Terada, S. Yoshida, O. Takeuchi, and H. Shigekawa, J. Phys.: Condens. Matter **22**, 264008 (2010).
17. C. Traum, P. Henzler, S. Lohner, H. Becker, D. Nabben, P. Gumbsheimer, C. Hinz, J. F. Lippmann, S. Mahapatra, K. Brunner, D. V. Seletskiy, and A. Leitenstorfer, Rev. Sci. Instrum. **90**, 123003 (2019).
18. P. Henzler, C. Traum, M. Holtkemper, D. Nabben, M. Erbe, D. E. Reiter, T. Kuhn, S. Mahapatra, K. Brunner, D. V. Seletskiy, and A. Leitenstorfer, Phys. Rev. Lett. **126**, 067402 (2021).
19. M. Garg and K. Kern, Science **367**, 411 (2020).
20. S. Grafström, J. Appl. Phys. **91**, 1717 (2002).
21. H. Timmers, A. Kowligy, A. Lind, F. C. Cruz, N. Nader, M. Silfies, G. Ycas, T. K. Allison, P. G. Schunemann, S. B. Papp, and S. A. Diddams, Optica **5**, 727 (2018).
22. R. Holzwarth, T. Udem, T. W. Hänsch, J. C. Knight, W. J. Wadsworth, and P. S. J. Russell, Phys. Rev. Lett. **85**, 2264 (2000).
23. D. J. Jones, Science **288**, 635 (2000).
24. M. Kakehata, H. Takada, Y. Kobayashi, K. Torizuka, Y. Fujihira, T. Homma, and H. Takahashi, Opt. Lett. **26**, 1436 (2001).
25. C. Chen, Y.-Y. Yin, and D. S. Elliott, Phys. Rev. Lett. **64**, 507 (1990).
26. Y.-Y. Yin, C. Chen, D. S. Elliott, and A. V. Smith, Phys. Rev. Lett. **69**, 2353 (1992).
27. M. Sheik-Bahae, Phys. Rev. B **60**, R11257 (1999).
28. A. Leitenstorfer, C. Fürst, A. Laubereau, W. Kaiser, G. Tränkle, and G. Weimann, Phys. Rev. Lett. **76**, 1545 (1996).